ORNL/TM-2019/1135

Partial Completion of Post-Irradiation Examination of the ORNL Samples

Lizhen Tan
Tianyi Chen
Oak Ridge National Laboratory

February 28, 2019

OAK RIDGE NATIONAL LABORATORY
MANAGED BY UT-BATTELLE FOR THE US DEPARTMENT OF ENERGY

DOCUMENT AVAILABILITY

Reports produced after January 1, 1996, are generally available free via US Department of Energy (DOE) SciTech Connect.

Website www.osti.gov

Reports produced before January 1, 1996, may be purchased by members of the public from the following source:

National Technical Information Service
5285 Port Royal Road
Springfield, VA 22161
Telephone 703-605-6000 (1-800-553-6847)
TDD 703-487-4639
Fax 703-605-6900
E-mail info@ntis.gov
Website http://classic.ntis.gov/

Reports are available to DOE employees, DOE contractors, Energy Technology Data Exchange representatives, and International Nuclear Information System representatives from the following source:

Office of Scientific and Technical Information
PO Box 62
Oak Ridge, TN 37831
Telephone 865-576-8401
Fax 865-576-5728
E-mail reports@osti.gov
Website http://www.osti.gov/contact.html

This report was prepared as an account of work sponsored by an agency of the United States Government. Neither the United States Government nor any agency thereof, nor any of their employees, makes any warranty, express or implied, or assumes any legal liability or responsibility for the accuracy, completeness, or usefulness of any information, apparatus, product, or process disclosed, or represents that its use would not infringe privately owned rights. Reference herein to any specific commercial product, process, or service by trade name, trademark, manufacturer, or otherwise, does not necessarily constitute or imply its endorsement, recommendation, or favoring by the United States Government or any agency thereof. The views and opinions of authors expressed herein do not necessarily state or reflect those of the United States Government or any agency thereof.

ORNL/TM-2019/1135
M3NA-17OR0204016

FY 2017 Consolidated Innovative Nuclear Research (CINR)
Nuclear Science User Facilities (NSUF)
Light Water Reactor Sustainability (LWRS)

PARTIAL COMPLETION OF POST-IRRADIATION EXAMINATION OF THE ORNL SAMPLES

Lizhen Tan and Tianyi Chen
Oak Ridge National Laboratory

Date Published: February 28, 2019

Prepared by
OAK RIDGE NATIONAL LABORATORY
Oak Ridge, TN 37831-6283
managed by
UT-BATTELLE, LLC
for the
US DEPARTMENT OF ENERGY
under contract DE-AC05-00OR22725

CONTENTS

LIST OF TABLES

LIST OF FIGURES

ACKNOWLEDGMENTS

This research was sponsored by the U.S. Department of Energy (DOE), Office of Nuclear Energy (NE), the FY 2017 Consolidated Innovative Nuclear Research (CINR) Nuclear Science User Facilities (NSUF) program and the Light Water Reactor Sustainability (LWRS) program. We gratefully acknowledge the support provided by Alison Hahn of DOE-NE and Rory Kennedy of Idaho National Laboratory for the NSUF access support and Keith Leonard of Oak Ridge National Laboratory (ORNL) for the research and development support of this project.

The authors are grateful to Kurt Terrani, NSUF technical leader of ORNL, for supporting this project and Kory Linton, Alicia Raftery, Ben Garrison, Clay Morris, Mark Delph, Patricia Tedder, and Joshua Schmidlin of ORNL for sample sorting, reception, and testing. Kevin Field and Xiang Chen of ORNL are appreciated for technical review of this report.

EXCUTIVE SUMMARY

A total of six Grade 92 and two 800H samples were identified and secured as the selected ORNL samples, which were irradiated in the High Flux Isotope Reactor (HFIR) of ORNL to 0.46–14.66 dpa at 400 to ~720°C. The Grade 92 is an optimized heat and named as G92-2b. The two 800H samples have one sample as the standard solution-annealed condition and the other sample as a thermos-mechanically processed (TMP) condition with a maximized fraction of low-Σ coincidence site lattice (CSL) boundaries.

Tensile tests were completed for the selected ORNL samples using the Irradiated Materials Examination and Testing (IMET) hot cell facility at ORNL. The G92-2b samples were tested at room temperature. The lower temperature irradiation at 400–496.7°C to 0.52–14.66 dpa resulted in minimal changes in tensile properties. However, the higher temperature irradiation at ~683.3–720°C to 0.46–14.63 dpa tended to reduce yield and tensile strength by about –136 to –311 MPa and plastic elongation with the increasing dose. The 800H and 800H-TMP samples were tensile-tested at their irradiation temperature 580°C, which showed >40% increase in yield and tensile strength with nearly 9% reduction in elongation for 800H-TMP compared with 800H.

Three of the selected ORNL samples, i.e., GB04 (7.44 dpa at ~490°C), GB05 (14.66 dpa at 496.7°C), and GB12 (14.63 dpa at ~720°C), were examined at LAMDA for Vickers hardness measurements and microstructural characterization by SEM and TEM. Vickers hardness was successfully measured on GB12, which was reduced by is – (112.4 ± 12.3) HV1 from the control sample. However, the Vickers hardness measurements were failed on GB04 and GB05 because the samples were polished too thin to eliminate the interference from the substrate (epoxy). The other half of the GB04 and GB05 will be polished for the hardness measurements, as well as nanoindentation studies.

Fractography by SEM indicated increased numbers of ductile dimples (or voids) with the increasing irradiation dose, while significantly increased numbers and sizes of dimples with the increasing irradiation temperature. TEM characterization exhibited the presence of $Cr_{23}C_6$, VN, and Laves precipitates at boundaries and matrix, which showed pronounced precipitate-dislocation interactions (pinning effect). Dense dislocations but limited dislocation loops were observed in the samples, which noticeably reduced in GB12. Additionally, some tiny partially amorphized spherical domains were observed in GB12, which had a normal body-centered cubic lattice parameter of 9Cr steels at the surround regions but ~11% smaller than the lattice parameter of the matrix away from the amorphized spherical domains. Further characterization will be pursued to clarify the new findings.

1. INTRODUCTION

Advanced alloys are desired to provide greater safety margins, design flexibility and economics compared to traditional reactor materials. Grade 92 ferritic-martensitic steel and austenitic Alloy 800/800H are two of the promising alloys interested by the current Advanced Radiation-Resistant Materials (ARRM) and Light Water Reactor Sustainability (LWRS) programs. However, systematic studies on neutron-irradiation induced changes in microstructures and mechanical properties are deficient for the alloys. The objective of this project is to develop correlations between microstructures and mechanical properties of the neutron-irradiated Grade 92 and Alloy 800/800H, based on the experimental results generated from this work. It is expected to develop broader correlations for these types of steels by comparing the results of this work with that of similar alloys such as Grade 91, Alloy 709 and type 304/316 stainless steels from literature and the ongoing studies, with the aid of thermodynamics, kinetics, and microstructural hardening modeling.

Samples of Grade 92 and Alloy 800H selected in this work were primarily irradiated in two test reactors for up to ~14 displacements per atom (dpa) at ~241–720°C. Samples of Grade 91, irradiated in the same reactors, were selected as references of Grade 92. Few samples from other two reactors will be included for comparison. Both irradiated and unirradiated samples from the same heat of the materials will be examined to elucidate the radiation-induced evolutions in microstructures, mechanical properties, and deformation mechanisms. To be more specific, mechanical properties such as tensile properties, modulus, hardness, and viscoplasticity will be measured through tensile, Vickers hardness and nanoindentation tests. Microstructural characterization of the samples will be carried out using the state-of-the-art instruments and techniques provided through the Nuclear Science User Facilities (NSUF). The obtained experimental results will then be used to establish the knowledgebase on the effects of alloy chemistry, thermomechanical-processing, and irradiation conditions on microstructures and mechanical properties of Grade 92 and Alloy 800H.

Outcomes of this project will include a comprehensive set of data including microstructures and mechanical properties of both irradiated and unirradiated samples of the interested steels, which will not only help understanding the essential performance of similar alloys, but more importantly to gain indispensable insights into the development of advanced alloys with superior radiation resistance. The outcomes can also serve as inputs and/or benchmarks for microstructural and mechanical property modeling of irradiated ferritic-martensitic and austenitic steels. The accomplishment of this project will directly benefit the LWRS program and bring values to the Advanced Reactor Technologies and Small Modular Reactors programs.

The selected samples irradiated in the High Flux Isotope Reactor (HFIR) of Oak Ridge National Laboratory (ORNL) have been tensile-tested and part of samples have been examined. This report summarizes the post-irradiation examination results of the ORNL samples.

2. SELECTED ORNL SAMPLES

2.1 SAMPLES

The selected ORNL samples include G92-2b and 800H samples irradiated to 0.46–14.66 dpa at 400 to ~720°C in the High Flux Isotope Reactor (HFIR) of ORNL, which are listed in Table 1, together with the alloy composition and condition in Table 2. The G92-2b is a heat of optimized Grade 92, which was developed under the Advanced Reactor Technologies (ART) program [1]. It showed improved strength and creep resistance compared with conventional Grade 92 such as NF616. The AR2 and HG1 samples are 800H and 800H-TMP (ThermoMechanical Processing), respectively, from the same heat as the Idaho National Laboratory (INL) samples that are to be examined in this project. The G92-2b samples are in type SS-J2 miniature tensile specimens with 16 × 4 × (<1) mm overall size and 5 × 1.2 × (<1) mm for the gauge section. The 800H and 800H-TMP samples are in type SS-3 miniature tensile specimens with 25.4 × 4.95 × 0.76 mm overall size and 7.62 × 1.52 × 0.76 mm for the gauge section.

Table 1. Selected ORNL samples.

Specimen type	Alloy	Sample ID	Planned Temperature (°C)	Temperature (°C)	Dose (dpa)
SS-J2	G92-2b	GB03	300	400	0.52
		GB04		~490	7.44
		GB05		496.7	14.66
		GB10	650	683.3	0.46
		GB11		~720	7.44
		GB12		~720	14.63
SS-3	800H	AR2	600	580	1.28
	800H-TMP	HG1			

Table 2. Compositions in weight percent (wt%) of the ORNL samples, with Fe as balance[*].

Alloy	Cr	Ni	Mn	Si	Ti	Al	V	W	Mo	Nb	C	N	B
G92-2b	8.9	0.10	0.47	0.14			0.23	1.9	0.43	0.11	0.087	0.045	<0.002
800H/800-TMP	20.42	31.59	0.76	0.13	0.57	0.50					0.069		

[*] The blank cells are the elements not measured or reported. Copper, phosphor, and sulfur contents were reported as 0.42%, 0.014%, and 0.001%, respectively in 800H/800H-TMP.

G92-2b was normalized at 1080°C for 1 h, followed by hot-rolling to 0.6”-thick plate from 1” at 1080°C and water quench, and tempered at 750°C for 2 h with air cooling. 800H was solution-annealed at 1177°C for 24 minutes per centimeter of thickness, followed by a water quench. 800H-TMP was based on 800H, subjected to ~6.6% thickness reduction by rolling at room temperature and then annealed at 1050°C for 1.5 h with water quench. The TMP led to a grain boundary engineering (GBE) effect to significantly increase the fraction of low-Σ coincidence site lattice (CSL) boundaries, e.g., nearly 70% (800H-TMP) and ~40% (800H) low-Σ CSL boundaries [2]. GBE with a significantly increased fraction of low-Σ CSL boundaries would benefit a variety of properties such as strength and resistance to creep, stress corrosion cracking, and oxidation [3]. The 800H-TMP exhibited noticeable enhancements in the resistance to thermal aging [4] and corrosion in supercritical water and high-temperature air [5,6,7,8]. Preliminary studies also showed more or less improvements in resistance to neutron irradiation [9,10]. Therefore, the pair of 800H/800H-TMP samples irradiated in a nearly identical condition, together with the pairs of 800H/800H-TMP samples from INL, were selected in this project to confirm and elucidate the beneficial effects of GBE/TMP on the neutron irradiation resistance of 800H.

2.2 IRRADIATION TEMPERATURES

Some of the irradiation temperatures are reported according to the analyzed results of the accompanied SiC temperature monitor samples irradiated with the selected samples, while the approximate temperatures with a "~" sign are estimated from extrapolation according to the available SiC temperature monitor results. Figure 1 shows the analyzed temperature from the available SiC temperature monitor samples in the same irradiation campaign as a function of irradiation dose in a logarithmic scale. Each dose has three temperature data points from the SiC samples at the top, middle, and bottom sections of irradiation capsules, which are not differentiated in the plot. The bottom section had relatively stable temperatures, while the top section had relatively large variations with increasing doses. The middle section generally had the highest temperatures, especially at higher doses.

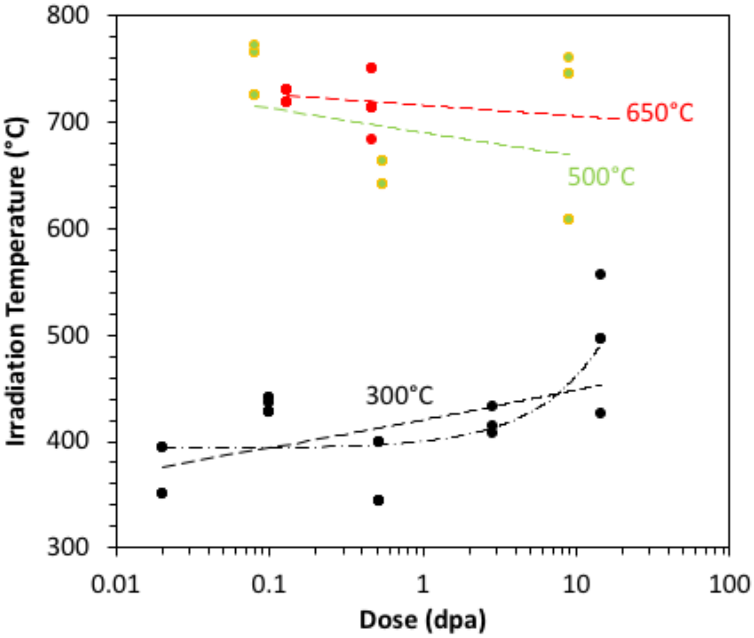

Figure 1. Irradiation temperature as a function of dose of steel samples irradiated with the G92-2b samples.

The dose-dependent irradiation temperature data are roughly fitted with a power function as shown in dashed lines in Figure 1, while the 300°C data also exhibited a better fitting by a linear function as shown in a dash-dot line. In general, the planned 300°C irradiation turns out to be above ~350°C and increasing with higher doses, especially for doses above 3 dpa. In contrast, the planned 500 and 650°C irradiations had similar irradiation temperatures, tending to slightly decrease with increasing doses. According to the Figure 1, it is expected that GB04 at the middle section of the irradiation capsule was irradiated at ~490°C, while GB11 and GB12 at the middle section of the irradiation capsule was irradiated at ~720°C. The irradiation temperatures were ~100–200°C and ~30–70°C higher than the planned 300 and 650°C. One of factors causing such large increases from the planned temperatures would be gamma heat generated from tungsten samples that were irradiated with the steel samples in the same capsules. The selected Grade 92 samples irradiated in the Advanced Test Reactor (ATR) of Idaho National laboratory were irradiated at temperatures in the range of 241–431°C, which will provide low-temperature properties to have an overall picture about radiation resistance of Grade 92.

The 800H and 800H-TMP were irradiated in a different irradiation campaign, which exhibited minimal difference between the planned and the analyzed irradiation temperatures.

3. TENSILE TEST RESULTS

Tensile test was conducted in the Irradiated Materials Examination and Testing (IMET) hot cell facility, using shoulder load at a strain rate of 0.001/s at room temperature.

3.1 G92-2B SAMPLES

Figure 2 shows the stress-strain curves of the selected G92-2b samples, together with the same heat unirradiated control sample, tested at room temperature. Part of the tensile testing curves were reported recently [11].

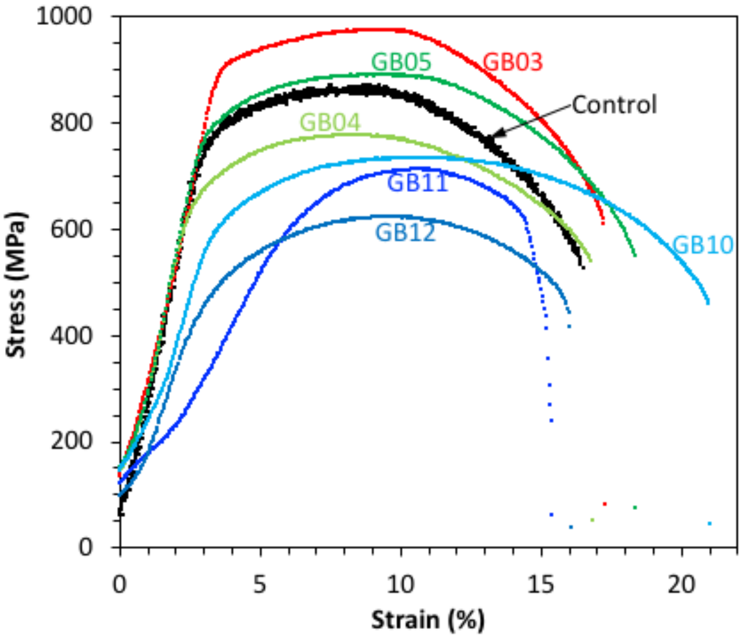

Figure 2. Stress-strain tensile curves of the selected G92-2b samples tested at room temperature.

By analyzing the curves, the tensile properties such as yield and tensile strength and uniform and total plastic elongation of the samples were obtained and are plotted in Figure 3 as a function of dose of the samples. The 0.52 dpa irradiation at 400°C resulted in small increases in yield and tensile strength by 115–153 MPa but without noticeable changes in uniform and total plastic elongation. The increased doses to 7.44 and 14.66 dpa at ~490–496.7°C caused small reductions of yield and tensile strength close to that of the control sample, with minimal changes or slight increases in uniform and total plastic elongation. In contrast, the 0.46 and 7.44 dpa irradiation at ~683.3–720°C consistently reduced some yield and tensile strength by about –136 to –168 MPa, with decreasing uniform and total plastic elongation with the increasing dose. The higher dose 14.63 dpa irradiation at ~720°C resulted in further decreases in yield and tensile strength, but without noticeable recovery of uniform and total plastic elongation.

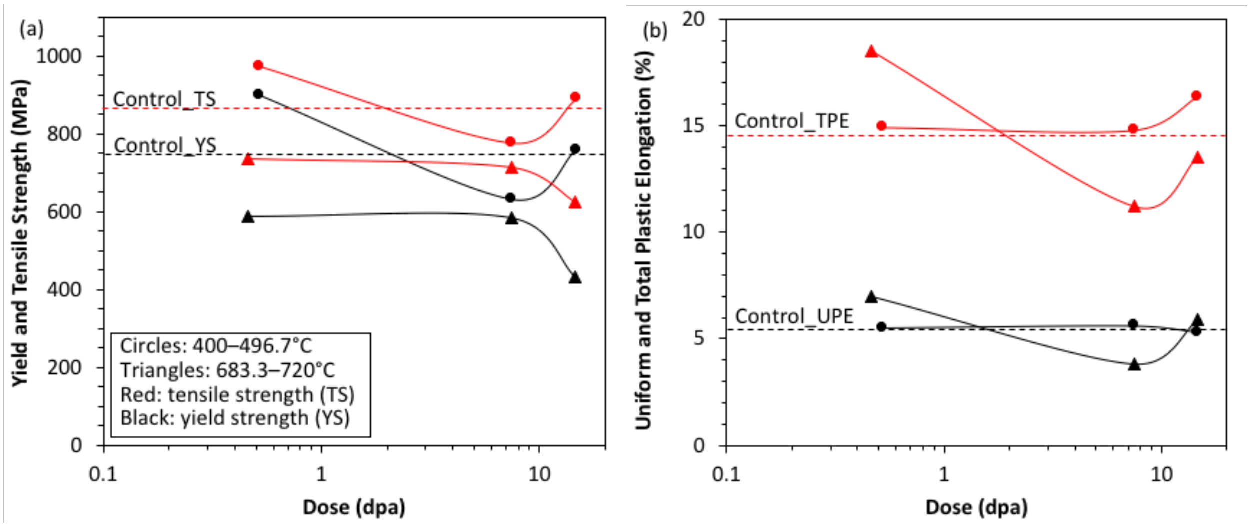

Figure 3. Dose-dependent (a) yield and tensile strength and (b) uniform and total plastic elongation of the selected G92-2b samples tested at room temperature.

3.2 800H/800H-TMP SAMPLES

Tensile testing of the 800H and 800H-TMP samples were tested at room temperature by another program. The tensile properties of the two samples are listed in Table 3, with the results reported by Nanstad et al. [12]. The tensile results tested at the irradiation temperature 580°C indicate noticeable increases in yield and ultimate (or tensile) strength by ~130–150 MPa, with little reductions in uniform and total elongation by about –0.7 to –1.1%. Hardness measurements and microstructural characterization of the two samples have not been performed, which will be pursued to correlate with the tensile properties.

Table 3. Tensile test results of 800H/800H-TMP samples[*].

Alloy	Sample	Yield strength (MPa)	Ultimate strength (MPa)	Uniform elongation (%)	Total elongation (%)
800H	AR2	272.0	362.4	8.05	12.9
800H-TMP	HG1	403.7	514.4	7.34	11.8

[*] The samples were irradiated in HFIR to 1.28 dpa at 580°C, which were tensile-tested at 580°C.

4. HARDNESS TEST RESULTS

Only GB04, GB05, and GB12 were received at the Low Activation Materials Design and Analysis (LAMDA) laboratory of ORNL from the IMET hot cell facility of ORNL. Therefore, only the three samples have been subjected to hardness measurements and microstructural characterization, presented in this and the next Sections.

4.1 VICKERS HARDNESS

The GB04, GB05, and GB12 samples, together with the same heat unirradiated control sample, were mounted in conductive epoxy and mechanically polished to a mirror finish. Vickers microhardness was measured on the polished samples at 0.1, 0.5, and 1 kgf with three or five measurements per condition. The optical images of representative indents are shown in Figure 4, which are not in the same scale bar. In contrast to the normal diamond shape of the Vickers indents on GB12 and that on GB04 at 0.1 kgf, the indents on the GB04 at the other loads and GB05 are in an abnormal star shape.

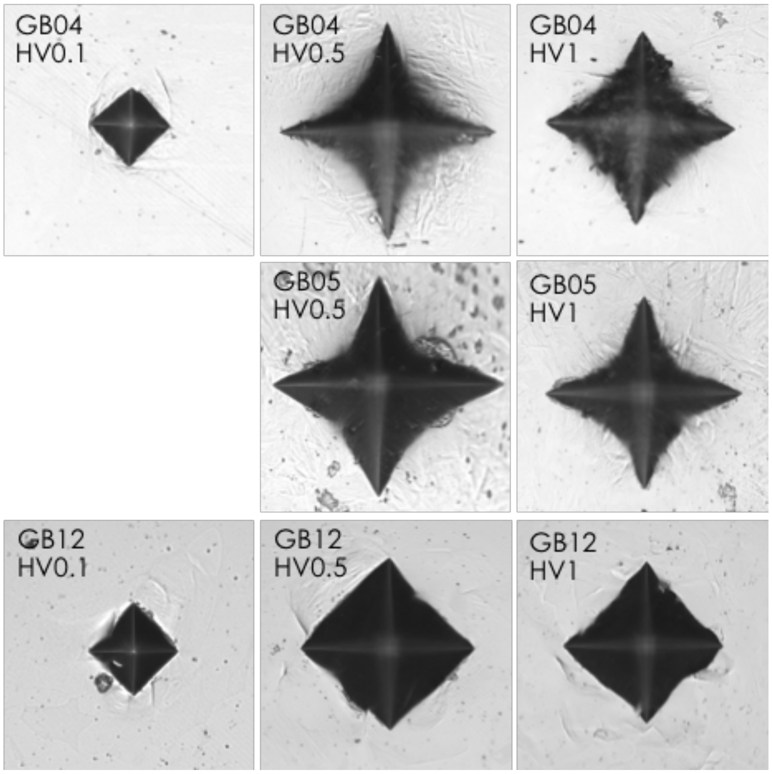

Figure 4. Optical images of representative indents on GB04, GB05, and GB12 illustrate the morphologies of the indents, which are not in the same scale bar.

The Vickers hardness as a function of the indentation depth of GB04, GB05, and GB12, together with the control sample and the epoxy, is plotted in Figure 5. The results of GB12 are normal, showing a small reduction in hardness from 167.6 ± 14.9 HV0.1 to 147.6 ± 11.1 HV1 with the increasing indentation depth (or load), which have small standard deviations roughly comparable to that of the control sample and epoxy. The hardness of GB12 is – (112.4 ± 12.3) HV1 reduced from the control sample. In contrast, the GB04 and GB05 had pronounced reductions in hardness with the increasing indentation depth, which have significant larger standard deviations. The depth-dependent hardness of both GB04 and GB05 is obviously approaching that of the epoxy. Therefore, the results of GB04 and GB05 were greatly influenced by the substrate, i.e., epoxy, because the two samples were polished too thin to have representative bulk hardness property of the samples, consequently resulting in the star shape indents on GB04 and GB05 as shown in Figure 4.

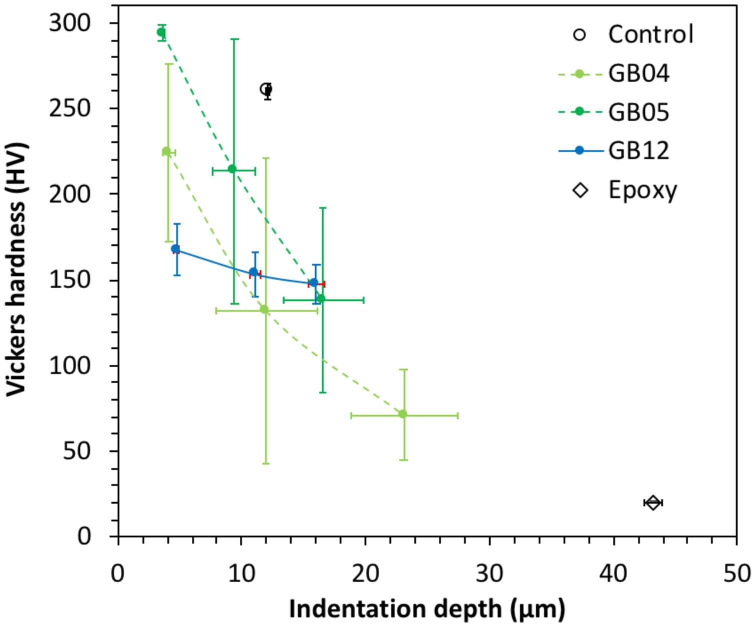

Figure 5. Stress-strain tensile curves of the selected G92-2b samples tested at room temperature.

4.2 NANOINDENTATION

Nanoindentation using Keysight Technologies Nano Indenter G200 was practiced on GB04 and GB05, which yielded abnormally low Young's modulus of 159 ± 20 and 116 ± 35 GPa, respectively. It indicates that such a lower level of load under nanoindentation was still influenced by the substrate epoxy. Therefore, the other part of the tensile-fractured sample of GB04 and GB05 is being requested for polishing and Vickers and nanoindentation studies, to be compared with the other selected samples and control sample.

5. MICROSTRUCTURAL CHARACTERIZATION

Microstructural characterization of the samples was primarily performed using scanning electron microscopy (SEM) and transmission electron microscopy (TEM).

5.1 FRACTOGRAPHY

Figure 6 shows fractography of the three received samples, i.e., GB04, GB05, and GB12, at LAMDA using SEM in a secondary electron imaging mode. Noticeably greater necking was observed for the ~490–496.7°C irradiated GB04 and GB05 compared with the ~720°C irradiated GB12, which is consistent with the tensile curves in Figure 2, showing a smaller difference between the total and uniform elongation of GB12 compared with GB04 and GB05. The higher irradiation dose of GB05 (14.66 dpa) increased ductile dimples (or voids) primarily in number density compared with GB04 (7.44 dpa). However, the higher irradiation temperature of GB12 (~720°C) significantly increased dimples in both density and size compared with GB05 (496.7°C) irradiated to about the same dose.

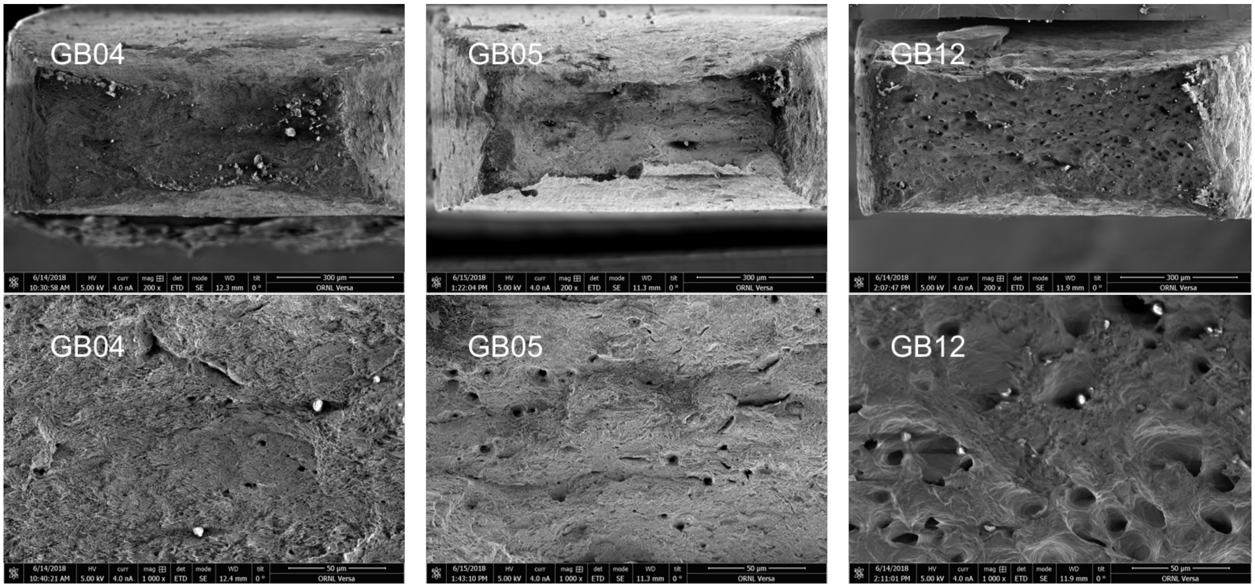

Figure 6. Fractography of the tensile-tested GB04, GB05, and GB12 samples.

5.2 IRRADIATED MICROSTRUCTURES

5.2.1 GB04 (7.44 dpa at ~490°C)

The irradiated microstructures at the tab section of the tensile-ruptured GB04 are shown in Figure 7, which is believed to be uninfluenced by the tensile stress because of the shoulder loading during the tensile test. The low-magnification bright-field (BF) scanning transmission electron microscopy (STEM) image in Figure 7a shows some precipitates, primarily at grain boundaries. The pre-existing tempered martensite seems noticeably reduced by the irradiation. Figure 7b from the large white-square-enclosed region in Figure 7a is a BF TEM image, showing two light grey $M_{23}C_6$ (M=Cr primarily) particles at a grain boundary. A dark Laves particle in a highly faulted structure is located beside one of the $M_{23}C_6$ particles. Figure 7c from the small white-square-enclosed region in Figure 7a is a high-resolution BF TEM image, showing the lattice image of the edge of the matrix precipitate. The inset of Figure 7c is a Fast Fourier

Transform (FFT) of the precipitate, which is not coherent with the matrix although it has not been indexed. Figure 7d is a BF STEM image taken from the [111] zone axis, which shows a high density of line dislocations. Radiation-induced dislocation loops are limited in this image compared to the line dislocations.

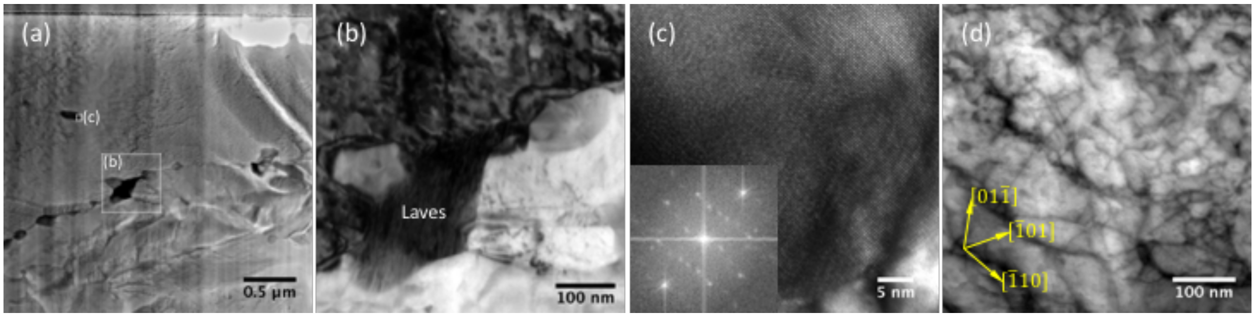

Figure 7. BF (a, d) STEM and (b-c) TEM images of GB04 showing its (a) overview, (b-c) precipitates, and (d) dislocations at the tab section of the tensile specimen.

Microstructural characterization from the gauge section and the fracture surface of GB04 was also performed. Figure 8a shows a BF STEM image from the gauge section with primarily $M_{23}C_6$ precipitates, together with some Laves particles, decorating grain boundaries. Lath structures with dislocations are seeable in Figure 8a. A matrix VN precipitate in a size of ~100 nm is shown in a BF STEM image Figure 8b, together with its selected area diffraction pattern as an inset. The weak reflections with some satellite reflections from the VN particle is partially coherent with the matrix (body-centered cubic – bcc) phase, which is identified as $[1\bar{2}0]_{VN} \parallel [1\bar{1}1]_{bcc}$ and $(422)_{VN} \parallel (011)_{bcc}$. The VN particle is interacting with a high-density of tangled dislocations, suggesting its pinning effect under tensile test. Figure 8c shows a BF STEM image from the fracture surface of GB04. Many dislocation-compiled polygonal cells in a size of ~0.4 µm formed in this region, which was resulted from the high stress in the necking zone.

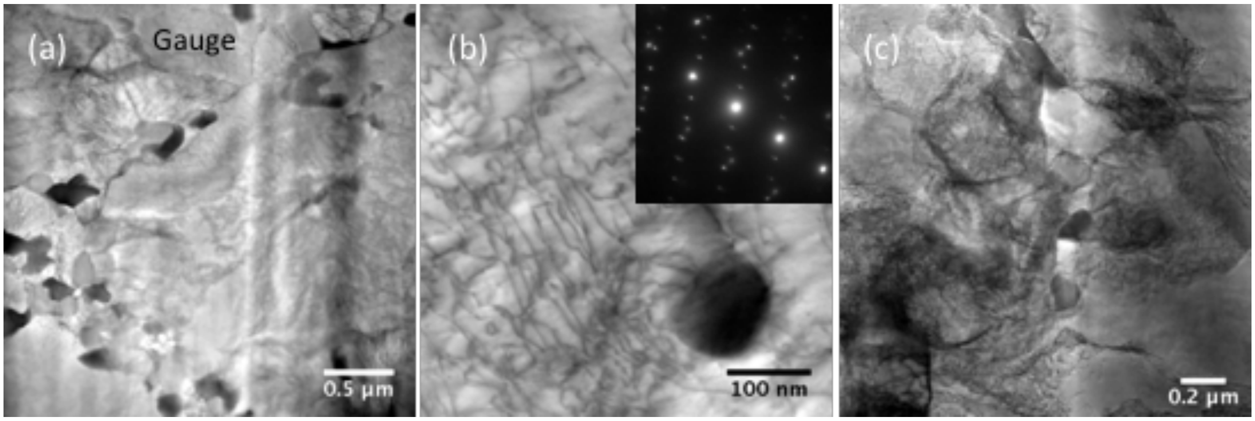

Figure 8. BF STEM images of GB04 at the (a-b) gauge and (c) fracture surface.

5.2.2 GB05 (14.66 dpa at 496.7°C)

The tab section microstructures of GB05 is shown in Figure 9, with an overview BF STEM image shown in Figure 9a, illustrating the presence of lath structures and dislocations. The high magnification BF STEM image in Figure 9b was taken from the [100] zone axis, which shows a high-density of line dislocations with limited dislocation loops. The BF TEM image in Figure 9c was taken from the lower part of Figure

9a, which shows four precipitates, labelled as p1 and p3–p5, decorating the lath boundaries and one precipitate, labelled as p2, in matrix. The high-resolution BF TEM images in Figure 9d-e exhibit examples of the precipitates p1 and p2, respectively, from Figure 9c. Their corresponding FFTs as shown in Figure 9d-e indicate p1 and p2 as $Cr_{23}C_6$ and VN type precipitates with lattice parameters of 1.057 and 0.431 nm, respectively. The $Cr_{23}C_6$ (p1) is coherent with the matrix (m1) on the right side of p1, i.e., $[110]_{Cr_{23}C_6} \parallel [100]_{bcc}$ and $(1\bar{1}1)_{Cr_{23}C_6} \parallel (011)_{bcc}$. while the VN (p2) is fully coherent with the matrix (m1) with both of them in the [100] zone axis.

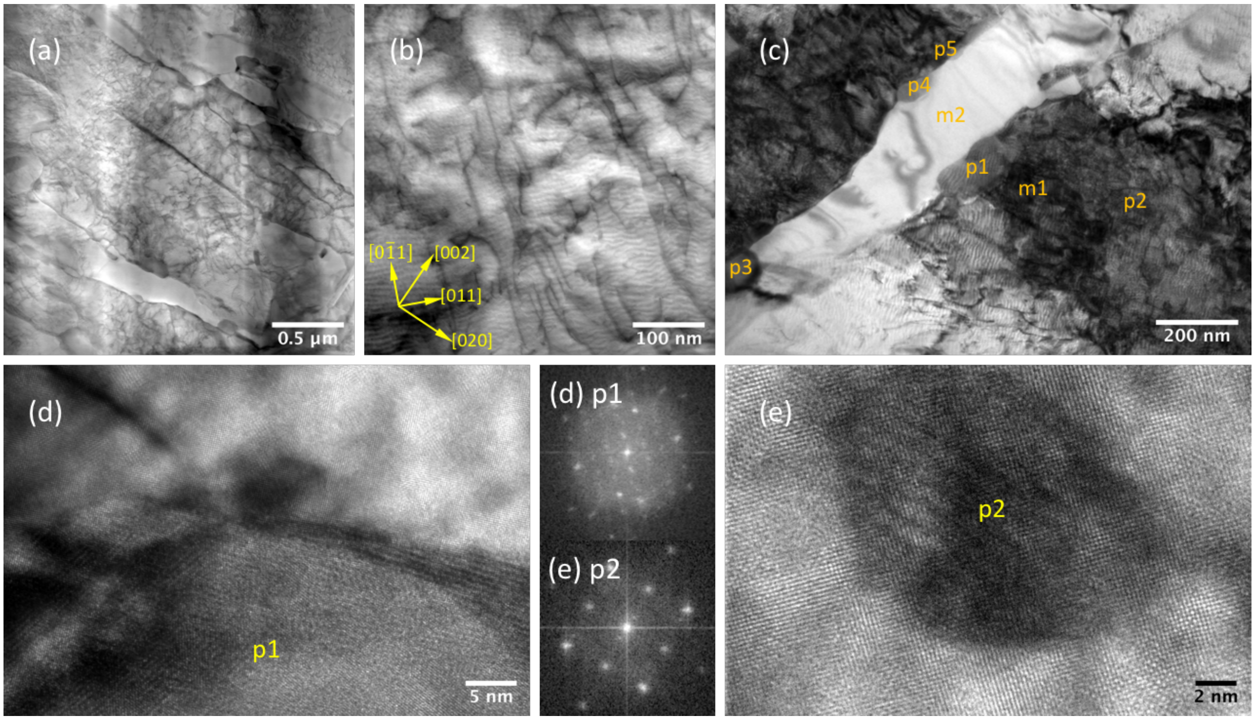

Figure 9. BF (a-b) STEM and (c-e) images and corresponding FFTs of (d-e) of GB05 at the tab section.

The BF STEM image of GB05 in the gauge section is shown in Figure 10a, with the left and lower part of the image on or close to a {111} zone axis, showing lath structures and dislocations. The upper-right side domain does not show lath structures, which is likely because it is off the zone-axis. Similar to GB04, tangled dislocations also developed in GB05 as shown in Figure 10b, with a precipitate, labelled as p, pinning dislocations. High-resolution BF TEM image of the precipitate (p) is shown in Figure 10c. The FFT inset of Figure 10c indicates good coherency with the matrix in the [111] zone axis, similar to that in the [100] zone axis as shown in Figure 9e.

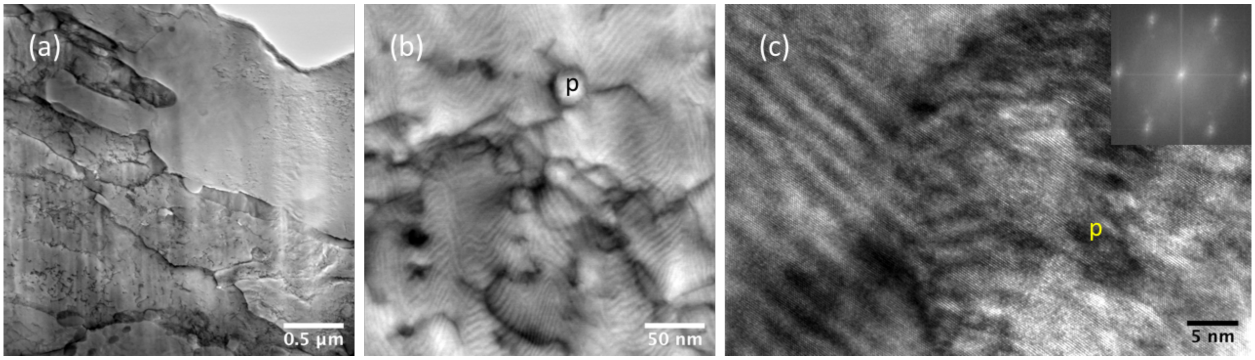

Figure 10. BF (a-b) STEM and (c) TEM images of GB05 at the gauge section.

5.2.3 GB12 (14.63 dpa at ~720°C)

Figure 11 shows the tab section microstructure of GB12. Lath structures were mostly diminished in the overview BF STEM image in Figure 11a. The higher magnification BF STEM image in Figure 11b was taken from the region near the top of Figure 11a, which exhibits a dense short dislocation sections in the [100] zone axis. Some bright spherical features were observed under BF STEM imaging condition, which is exemplified in Figure 11c. The high-resolution STEM image of one of the bright features is shown in Figure 11d, illustrating amorphous center and crystalline interface with the matrix. The FFT of the image (not shown here) indicates a singular set of bcc structure, the same as the matrix, with a diffused center suggesting the presence of amorphous from the center of the spherical center. Lattice parameter analyses from the FFTs of multiple locations in the matrix away from the bright spherical features yielded 0.3224 ± 0.0068 nm, which is relaxed to the general Fe-bcc lattice parameter of 0.2862 ± 0.0045 nm at the regions adjacent to the bright amorphized spherical features.

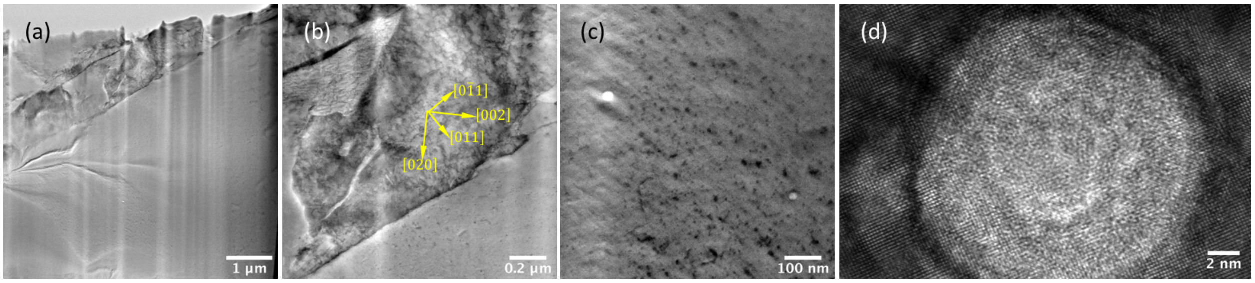

Figure 11. BF (a-b) STEM and (c-e) images and corresponding FFTs of (d-e) of GB12 at the tab section.

The microstructures of GB12 at the gauge section and the fracture surface are shown in Figure 12a-c and d, respectively. The BF STEM images of the gauge section in Figure 12a-b exhibit primarily prior-austenite grain boundaries with some partially retained lath structures, populated with dense short dislocation sections. Only a few sub-micrometer "particles", e.g., the one in Figure 12a below the "p" label, were observed in GB12. The high-resolution BF TEM of the particle-p, together with its FFT as the inset in Figure 12c, suggests that the particle-p is a ferrite domain/grain with a lattice parameter of 0.2908 nm. The microstructure at the fracture surface, where experienced the highest stress during the tensile test at room temperature, shows pronounced lath structures in Figure 12d.

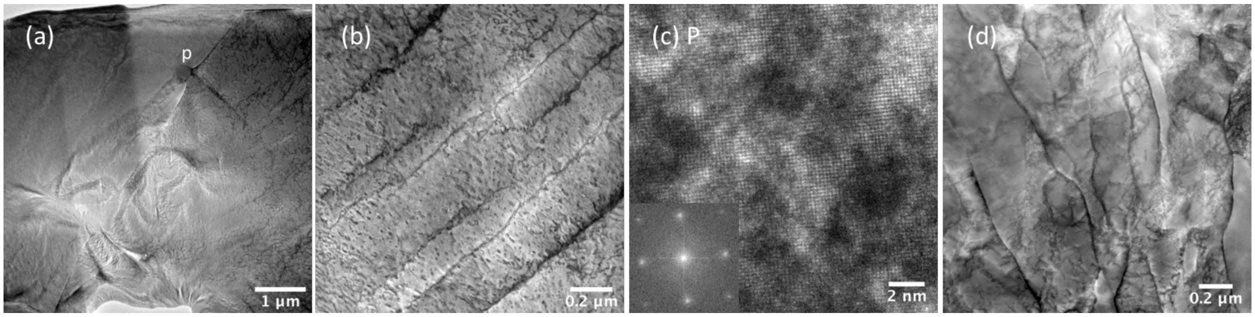

Figure 12. BF STEM images of GB12 at the (a-b) gauge and (c) fracture surface.

6. CONCLUSION

A total of six Grade 92 and two 800H samples were identified and secured as the selected ORNL samples, which were irradiated in the HFIR to 0.46–14.66 dpa at 400 to ~720°C. The Grade 92 is an optimized heat and named as G92-2b. The two 800H samples have one sample as the standard solution-annealed condition and the other sample as a TMP condition with a maximized fraction of low-Σ CSL boundaries.

Tensile tests were completed for the selected ORNL samples using the IMET hot cell facility. The G92-2b samples were tested at room temperature. The lower temperature irradiation at 400–496.7°C to 0.52–14.66 dpa resulted in slight hardening or softening without noticeable changes in uniform and total plastic elongation. In contrast, the higher temperature irradiation at ~683.3–720°C to 0.46–14.63 dpa tended to reduce yield and tensile strength by about –136 to –311 MPa and plastic elongation with the increasing dose. The 800H and 800H-TMP samples were tensile-tested at their irradiation temperature 580°C, which showed >40% increase in yield and tensile strength with nearly 9% reduction in elongation for 800H-TMP compared with 800H.

Three of the selected ORNL samples, i.e., GB04 (7.44 dpa at ~490°C), GB05 (14.66 dpa at 496.7°C), and GB12 (14.63 dpa at ~720°C), were examined at LAMDA. Vickers hardness was successfully measured on GB12, which was reduced by – (112.4 ± 12.3) HV1 from the control sample. However, the Vickers hardness measurements were failed on GB04 and GB05 because the samples were polished too thin to eliminate the interference from the substrate (epoxy). The other half of the GB04 and GB05 will be polished for the hardness measurements, as well as nanoindentation studies.

Fractography of GB04, GB05, and GB12 by SEM indicated increased ductile dimples (or voids) primarily in number density with the increasing irradiation dose, while significantly increased dimples in both density and size with the increasing irradiation temperature. Microstructural characterization by TEM exhibited the presence of $Cr_{23}C_6$, VN, and Laves precipitates at boundaries and matrix, which showed pronounced precipitate-dislocation interactions (pinning effect). Dense dislocations but limited dislocation loops were observed in the samples, which noticeably reduced in the higher-temperature-irradiated GB12. Additionally, some tiny partially amorphized spherical domains were observed in GB12, which had a normal bcc lattice parameter of 9Cr steels at the surround regions but ~11% smaller than the lattice parameter of the matrix away from the amorphized spherical domains. Further characterization will be pursued to clarify the new findings.

REFERENCE

---

[1] L. Tan, P.J. Maziasz, T.-L. Sham, Report on the optimization and testing results of advanced ferritic/martensitic alloys, ORNL/TM-2012/288, September 14, 2012.

[2] L. Tan, T.R. Allen, An electron backscattered diffraction study of grain boundary-engineered Incoloy alloy 800H, Metall. Mater. Trans. A 36 (2005) 1921–1925.

[3] L. Tan, T.R. Allen, J.T. Busby, Grain boundary engineering for structure materials of nuclear reactors, J. Nucl. Mater. 441 (2013) 661–666.

[4] L. Tan, L. Rakotojaona, T.R. Allen, R.K. Nanstad, J.T. Busby, Microstructure optimization of austenitic alloy 800H (Fe–21Cr–32Ni), Mater. Sci. Eng. A 528 (2011) 2755–2761.

[5] L. Tan, K. Sridharan, T.R. Allen, The effect of grain boundary engineering on the oxidation behavior of Incoloy alloy 800H, J. Nucl. Mater. 348 (2006) 263–271.

[6] L. Tan, K. Sridharan, T.R. Allen, Altering corrosion response via grain boundary engineering, Mater. Sci. Forum 595–598 (2008) 409–418.

[7] L. Tan, K. Sridharan, T.R. Allen, R.K. Nanstad, D.A. McClintock, Microstructure tailoring for property improvements by grain boundary engineering, J. Nucl. Mater. 374 (2008) 270–280.

[8] L. Tan, T.R. Allen, Y. Yang, Corrosion behavior of alloy 800H (Fe–21Cr–32Ni) in supercritical water, Corros. Sci. 53 (2011) 703–711.

[9] R.K. Nanstad, D.A. McClintock, D.T. Hoelzer, L. Tan, T.R. Allen, High temperature irradiation effects in selected Generation IV structural alloys, J. Nucl. Mater. 392 (2009) 331–340.

[10] L. Tan, J.T. Busby, H.J.M. Chichester, K. Sridharan, T.R. Allen, Thermomechanical treatment for improved neutron irradiation resistance of austenitic alloy (Fe–21Cr–32Ni), J. Nucl. Mater. 437 (2013) 70–74.

[11] A. Raftery, L. Tan, H. Sakasegawa, K. Linton, Tensile testing of irradiated Grade 92 ferritic-martensitic steels at the IMET hot cell facility, ORNL/LTR-2018/499, April 2018.

[12] R.K. Nanstad, D.A. McClintock, D.T. Hoelzer, L. Tan, T.R. Allen, High temperature irradiation effects in selected Generation IV structural alloys, J. Nucl. Mater. 392 (2009) 331–340.